

Acoustic pulsation for heat transfer abatement in supersonic channel flow

Cite as: Phys. Fluids **33**, 035104 (2021); <https://doi.org/10.1063/5.0037078>

Submitted: 10 November 2020 . Accepted: 05 January 2021 . Published Online: 02 March 2021

 Iman Rahbari,  Beni Cukurel, and  Guillermo Paniagua



View Online



Export Citation



CrossMark

Physics of Fluids

SPECIAL TOPIC: Tribute to
Frank M. White on his 88th Anniversary

SUBMIT TODAY!

Acoustic pulsation for heat transfer abatement in supersonic channel flow

Cite as: Phys. Fluids **33**, 035104 (2021); doi: 10.1063/5.0037078

Submitted: 10 November 2020 · Accepted: 5 January 2021 ·

Published Online: 2 March 2021



View Online



Export Citation



CrossMark

Iman Rahbari,^{1,a)} Beni Cukurel,^{2,b)} and Guillermo Paniagua^{1,c)}

AFFILIATIONS

¹School of Mechanical Engineering, Purdue University, West Lafayette, Indiana 47907, USA

²Aerospace Engineering Department, Technion-Israel Institute of Technology, Technion City, Haifa 3200003, Israel

^{a)}Author to whom correspondence should be addressed: irahbari@purdue.edu

^{b)}bcukurel@technion.ac.il

^{c)}gpaniagua@purdue.edu

ABSTRACT

The impact of periodic pulsation normal to the flow passage on the heat and momentum transport is studied using direct numerical simulations. The selected test case is the fully developed supersonic turbulent flow at Reynolds numbers $Re_b = \bar{\rho}_b \bar{U}_b \delta / \bar{\mu}_{\text{wall}} = 3000$ and 6000 and Mach number $M_d = \bar{U}_d / \bar{c}_d \approx 1.5$, bounded by isothermal walls. The pulsation is introduced by imposing a time-periodic uniform body-force in the spanwise directions, mimicking two acoustic drivers placed on the side-walls that are operating with a 180° phase difference. Results indicate that the spanwise pulsation at a *moderate* forcing amplitude, with the spanwise velocity oscillation amplitude $\tilde{W}_d \approx 12\%$ of bulk streamwise velocity or $\tilde{W}_d^+ = \tilde{W}_d / u_\tau \approx 2$, can create about 8% reduction in the Nusselt number (Nu), as well as in the skin friction coefficient (C_f), if applied at the optimal pulsation period $\mathcal{T}^+ = \mathcal{T} u_\tau^2 / \bar{\nu}_{\text{wall}}$ within $[173, 346]$, where $\mathcal{T} = 2\pi / \omega_f$. The excitation outside this band fails to achieve such high levels of modulations in heat and momentum transport processes near the walls. Visualizing the instantaneous temperature field reveals a periodic tilting of the near-wall turbulent structures that is translated into a decay in the energy of the streamwise vortices and an increase in the mean spanwise distance of such structures. The effect of the excitation on reducing the turbulent heat flux and Reynolds shear stress is studied, and the resulting streaming temperature and velocity profiles are discussed.

Published under license by AIP Publishing. <https://doi.org/10.1063/5.0037078>

I. INTRODUCTION

The present study focuses on the physical processes underlying the pulsating turbulent boundary layers. The potential application of the findings provides a novel technique to modulate the flow and *reduce* the convective heat transfer. Hence, this technology may further increase the maximum allowable incoming flow temperature of future thermal system components, therefore improving the performance of the entire system. To this aim, we apply the period pulsation normal to the flow, in the *spanwise direction* (i.e., z -direction in Fig. 1), and characterize its effect on the heat and momentum transport. This mechanism is expected to *reduce the heat transfer and drag*, as it shares similarities with the Spanwise Wall Oscillation (SWO) mechanism, which has been studied extensively for drag reduction in low-speed flows.

Jung *et al.*¹ introduced the spanwise wall oscillation for drag control and found an optimal oscillation period of $\mathcal{T}^+ = \mathcal{T} u_\tau^2 / \nu = 100$ for drag reduction in an incompressible channel flow. Laadhari and co-workers² conducted a series of experiments and observed a reduced

velocity gradient near the oscillating wall. Thereafter, the Choi, DeBisschop, and Clayton³ experiment reported a sustained drag reduction using this technique. Since then, there has been an abundance of numerical and experimental research on the drag reduction using SWO in incompressible flows. The most notable findings are summarized by Karniadakis and Choi⁴ and Quadrio.⁵ Recently, Yao and Hussain⁶ performed direct numerical simulations (DNSs) to study the drag reduction using the spanwise wall oscillation in a supersonic turbulent channel flow and proposed scaling relations to connect the compressible and incompressible cases.

Although the spanwise wall oscillation has shown encouraging results in theory, implementing such a technique in most engineering systems is not practical. Several alternative mechanisms have been proposed to mimic this process without requiring an oscillating wall. Berger *et al.*⁷ numerically evaluated the application of Lorenz force to create a small flow motion, adjacent to the wall, and Breuer, Park, and Heno⁸ experimentally investigated this idea and achieved 10% drag reduction. The efficiency of this technique is particularly very poor

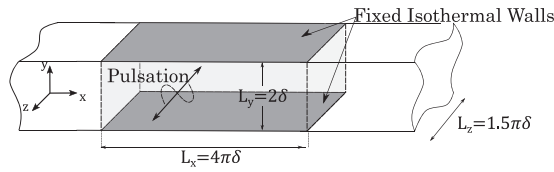


FIG. 1. Proposed setup to study the acoustic excitation in the spanwise direction. Acoustic drivers are active in the entire shaded area modeled via the forcing function of form (1).

($\approx 0.01\%$), mainly because of low electrical conductivity of the fluid, making it infeasible in most aerothermal applications. Jukes and co-workers⁹ experimentally created an oscillating forcing near the wall via plasma actuators and Ricco and Hahn¹⁰ numerically explored using small rotating discs flush-mounted on the horizontal walls, and both demonstrated a drag reduction in low-speed channel flows.

Another configuration Jung *et al.*¹¹ and Akhavan *et al.*¹¹ numerically studied involves an *oscillating cross flow*, with the amplitude as high as 80% of the streamwise flow-rate, in a turbulent channel flow, and it showed up to 40% drag reduction at the optimal specific oscillation frequency. Decreasing the amplitude of cross flow oscillation to the half reduced the drag reduction by a factor of four. Recently, Cannata, Cafiero, and Iuso¹² used an array of synthetic jets mounted on the vertical wall to apply an oscillating forcing normal to the flow and also allowed for a variation in the streamwise direction. They observed a skin friction reduction up to 20% in a fully developed low-speed turbulent channel flow. Therefore, implementing an oscillating pressure gradient in the spanwise direction seems to give equally promising results, as the SWO, while offering the much needed flexibility for practical aerothermal applications.

For instance, one can exploit the high-amplitude pulsations that exist intrinsically in the flow,¹³ for example, in turbocharger turbines¹⁴ at specific frequencies depending on the engine rotation speed¹⁵ and a Rotating Detonation Combustor (RDC)¹⁶ downstream in a gas turbines plant, or it can be generated externally, for example, via sirens¹⁷ or synthetic jets.¹²

In this study, we use DNSs to investigate applying a periodic forcing perpendicular to a supersonic turbulent flow and demonstrate a reduction in heat transfer and skin friction. The uniform forcing is applied to the entire volume of the fluid in the spanwise direction (z -direction in Fig. 1), while keeping the walls fixed, creating an oscillatory motion superimposed on the background turbulent flow. We particularly focus on moderate levels of pulsation where the amplitude of oscillating spanwise velocity at the channel center is $\tilde{W}_d \approx 12\%$ of bulk streamwise velocity or $\tilde{W}_d^+ = \tilde{W}_d/u_\tau \approx 2.0 - 2.2$, where $u_\tau = \sqrt{\tau_{\text{wall}}/\rho_{\text{wall}}}$. This is inspired by Quadrio and Ricco¹⁸ who showed this range of amplitude of wall oscillation velocity delivers the maximum *net* gain in terms of drag reduction, in an incompressible channel flow, while requiring a minimal input power. Moreover, this condition is considered to avoid very large oscillation amplitudes that may not be achieved effectively in practice.

Morkovin's hypothesis suggests that, in non-hypersonic boundary layers, the coupling between the pressure and thermal fields primarily occurs through mean variations of temperature, density, and viscosity.¹⁹ Several transformations have been proposed to remove this coupling and explain the flow field inside a compressible boundary

layer using observations corresponding to the incompressible flows.^{20,21} Van Driest's transformation provides an accurate description of a compressible boundary layer's velocity profile over an adiabatic wall.²² Trettel and Larsson²³ derived a semi-local scaling that can be applied accurately to the isothermal wall conditions. More recently, Volpiani *et al.*²⁴ proposed a new transformation to collapse the velocity profiles at different Mach numbers using a data-driven approach. In this research, we only focus on one Mach number, and therefore, applying such transformation may not be necessary. We invite the readers to consider collapsing the results of different flow conditions with the suggested transformations.

II. PROBLEM FORMULATION

The proposed test case to explore the effect of spanwise excitation on a supersonic turbulent flow comprises repeating identical units of length L_x . Each unit includes a duct with an array of pulsating sources mounted on both side-walls operated 180° out of phase. A schematic view of this setup is shown in Fig. 1. Thanks to the geometrical periodicity, only one unit needs to be simulated, and the periodic boundary conditions are imposed in the streamwise direction. Complexities arising from the boundary layer formed on the side-walls are avoided by limiting the scope of the present study to the mid-span region and implementing the periodic boundary condition in the spanwise direction. Therefore, the simplified computational setup includes two parallel plates of length L_x and width L_z separated by distance 2δ . The effect of pulsating sources is modeled with an external forcing as follows:

$$\vec{f}_f(\mathbf{x}, t) = A_f \sin(\omega_f t) \hat{e}_z, \quad (1)$$

where A_f indicates the forcing amplitude and ω_f is the excitation frequency. Because the drivers operate out of phase, the forcing only has one spanwise component. It is assumed that all points along the spanwise direction instantly feel the perturbations. This is possible due to the negligible "mean Mach number" in the spanwise direction.

III. NUMERICAL METHOD

Continuity, momentum, and energy equations for compressible flows in the Cartesian coordinate system read

$$\begin{aligned} \frac{\partial \rho}{\partial t} + \frac{\partial}{\partial x_j} (\rho u_j) &= 0, \\ \frac{\partial}{\partial t} (\rho u_i) + \frac{\partial}{\partial x_j} (\rho u_i u_j) &= -\frac{\partial p}{\partial x_i} + \frac{1}{Re} \frac{\partial}{\partial x_j} (\tau_{ij}) + f_i, \\ \frac{\partial E}{\partial t} + \frac{\partial}{\partial x_j} [(E + p)u_j] &= \frac{1}{Re} \frac{\partial}{\partial x_j} \left(k \frac{\partial T}{\partial x_j} \right) \\ &\quad + \frac{1}{Re} \frac{\partial}{\partial x_k} (\tau_{jk} u_j) + f_i u_i, \end{aligned} \quad (2)$$

where (x_1, x_2, x_3) or (x, y, z) represent the streamwise, wall-normal, and spanwise directions. The viscous stress tensor (τ^{ij}) and total energy (E) are

$$\begin{aligned} \tau_{ij} &= \mu \left(\frac{\partial u_i}{\partial x_j} + \frac{\partial u_j}{\partial x_i} - \frac{2}{3} \frac{\partial u_k}{\partial x_k} \delta_{ij} \right), \\ E &= \frac{p}{\gamma - 1} + \frac{1}{2} \rho u_i u_i, \end{aligned} \quad (3)$$

where the dynamic viscosity follows the exponential form $\mu/\mu_{\text{wall}} = (T/T_{\text{wall}})^{0.7}$. Wall temperature, T_{wall}^* , speed of sound and molecular viscosity at wall temperature, c_{wall}^* and μ_{wall}^* , bulk density ρ_b^* , and channel half-width δ^* are taken as the reference values for temperature, velocity, viscosity, density, and length scales, respectively. The equation of state, therefore, takes the form $p = \rho T/\gamma$. This non-dimensionalization is adopted following the work of Coleman, Kim, and Moser.²⁵

The term f_i on the right side of Eq. (2) represents a volume force, and $f_i u_i$ corresponds to the work applied on the flow by this force. At each time-step, the bulk velocity, U_b , is determined by $U_b = \int_V \rho u dV / \int_V \rho dV$, where V represents the entire volume of the channel. The volume forcing, f_i , is added uniformly to the entire domain if U_b deviates from the target value, $U_{b,\text{target}}$ in order to keep U_b , and consequently, the mass flow-rate, constant. In all cases studied here, $U_{b,\text{target}} = 1.5$. This procedure is commonly followed for simulation of turbulent channel flows.^{25–28} In the spanwise direction, the term f_3 is equal to the external forcing function defined in (1), while f_2 remains zero at all time.

A sixth-order compact finite difference method based on a staggered grid arrangement, proposed by Nagarajan, Lele, and Ferziger,²⁹ is used for spatial discretization of the above-mentioned equations, and the time-advancement is carried out via a third-order Runge–Kutta method. The grid is uniform in the x - and z -direction, while in the y -direction, it follows $y = 1 + \tanh(\alpha\eta)/\tanh(\alpha)$, where $\alpha = 2.5$ and η is the uniform distribution $\in [-1, 1]$. Metrics are calculated using the same spatial discretization.³⁰ This solver has been previously validated for the supersonic channel flow configuration in our previous publication,²⁸ and results are in good agreement with the reference data reported by Coleman, Kim, and Moser²⁵ in both first- and second-order turbulent statistics.

IV. RESULTS

We perform DNS of fully developed turbulent supersonic flow within isothermal walls at Mach numbers $M_{cl} = \bar{U}_{cl}/\bar{c}_{cl} = 1.49$ and

1.47 and Reynolds numbers $Re_b = \bar{\rho}_b \bar{U}_b \delta / \bar{\mu}_{\text{wall}} = 3000$ and 6000, respectively. This working condition corresponds to a heat exchanger with a channel of 2 cm height. The total absolute pressure upstream is 4.5 kPa (for $Re_b = 3000$) and 9 kPa (for $Re_b = 6000$). The temperature ratio between the hot flow and colder walls is 1.94; in all the simulations, the walls are kept isothermal at 300 K. The computational domain has the size $\Omega: L_x \times L_y \times L_z = 4\pi\delta \times 2\delta \times 1.5\pi\delta$, which is discretized using $N_x \times N_y \times N_z = 144 \times 128 \times 96$ grid points, in the low-Reynolds cases (cases A0 to A7). This corresponds to the resolution $(\Delta x^+, \Delta y_{\text{min}}^+, \Delta z^+) \approx (19, 0.24, 10.7)$ based on wall units where $(\cdot)^+ = (\cdot)u_\tau/\bar{\nu}_{\text{wall}}$, and the reference variables are calculated in the unexcited case. Simulations are performed at seven different pulsation frequencies, chosen such that the resulting Stokes layer thickness falls at different heights of the channel. A detailed description of these simulations is reported in Table I, cases A0 to A7. Simulations F0 and F1 with finer grids, using 1.5 times more grid points in each direction, are performed to ensure the results are independent of grid sizes. Time-averaged skin friction and heat flux show minimal deviation from A0 and A3 cases, respectively. The instantaneous flow fields, with the finer grid, are used for more precise visualization of the near-wall structures.

In the high-Reynolds number configuration, cases R0 to R3, a grid of size $N_x \times N_y \times N_z = 288 \times 256 \times 192$ has been adopted, which yields the resolution $(\Delta x^+, \Delta y_{\text{min}}^+, \Delta z^+) \approx (17.69, 0.22, 9, 97)$. Table I summarizes the simulation parameters and the associated Stokes boundary layer thickness where $\delta_s = \sqrt{2\nu_{\text{wall}}/\omega_f}$, as well as its corresponding non-dimensional form $\delta_s^+ = \delta_s u_\tau / \bar{\nu}_{\text{wall}}$ in wall units. As shown earlier, in all the cases studied in this manuscript, the amplitude of the spanwise velocity pulsations is kept approximately constant resulting in a dimensionless spanwise velocity amplitude of $\bar{W}_d^+ \approx 2.0$ – 2.2 at the channel center.

Three simulations, namely, A0, F0, and R0, do not include spanwise forcing and serve as the *reference unexcited solutions*. Time-averaged streamwise velocity, density, and temperature, spatially averaged in the streamwise and spanwise directions for these cases, are

TABLE I. Simulation parameters for the acoustic excitation normal to the flow in the spanwise direction for a supersonic channel flow at $M_{cl} = 1.49$ and 1.47.

Case	Re_b	A_f	$\mathcal{F} = 2\pi/\omega_f$	$N_x \times N_y \times N_z$	$\delta_s^+ = \delta_s u_\tau / \bar{\nu}_{\text{wall}}$
A0	3000	0	...	$144 \times 128 \times 96$...
A1	3000	0.20	5	$144 \times 128 \times 96$	5.2
A2	3000	0.10	10	$144 \times 128 \times 96$	7.4
A3	3000	0.05	20	$144 \times 128 \times 96$	10.5
A4	3000	0.025	40	$144 \times 128 \times 96$	14.8
A5	3000	0.0125	80	$144 \times 128 \times 96$	21.0
A6	3000	0.0083	120	$144 \times 128 \times 96$	25.7
A7	3000	0.0062	160	$144 \times 128 \times 96$	29.7
F0	3000	0	...	$216 \times 192 \times 144$...
F1	3000	0.05	20	$216 \times 192 \times 144$	10.5
R0	6000	0	...	$288 \times 256 \times 192$...
R1	6000	0.20	5	$288 \times 256 \times 192$	6.91
R2	6000	0.10	10	$288 \times 256 \times 192$	9.8
R3	6000	0.05	20	$288 \times 256 \times 192$	13.8

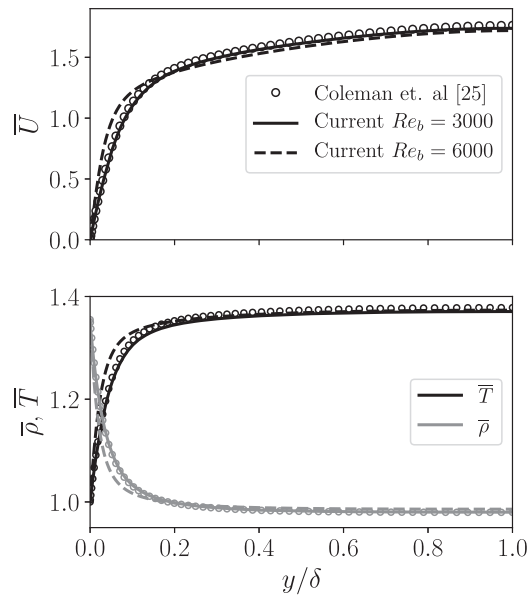


FIG. 2. Time-averaged streamwise velocity (left), density, and temperature (right) profiles for the unexcited cases at $Re_b = 3000$ and $M_{cl} = 1.49$ (open circles from Coleman, Kim, and Moser²⁵ and solid lines from the current simulations), as well as at $M_{cl} = 1.47$ and $Re_b = 6000$ (dashed-lines). Results are spatially averaged in the spanwise and streamwise directions.

plotted in Fig. 2, along with the profiles reported by Coleman, Kim, and Moser²⁵ (at $Re_b = 3000$ and $M_{cl} = 1.49$) for comparison.

Comparing A0, F0, and R0 cases against the acoustically excited simulations helps isolate the effect of the perturbation on the flow. Simulations in each of the A, F, and R category are initialized with the same flow field obtained from the base flow calculations. All other parameters, including the time-step size and grid distribution, are kept similar.

A. Temporal evolution of perturbations

Since the boundary layer excitation is applied via imposing an external forcing introduced in Eq. (1), monitoring the resulting spanwise velocity perturbations, $\delta w = w_{\text{excited}} - w_{\text{unexcited}}$, can give a better understanding on how this forcing is translated into sensible flow quantities. Figure 3 (right column) indicates the history of the spatially averaged spanwise velocity perturbations at the channel center, $y^+ \approx 215$. In all these cases, the velocity perturbation amplitude starts with oscillatory, yet purely positive, values and eventually decays to oscillations around zero in the limit-cycle, after about $t \approx 480$. Wave-height (min-to-max value) in each case is reported in Fig. 3 (right), which, owing to the condition $A_f \mathcal{T} = 1$, lies $\in [0.318, 0.356]$. Therefore, in all A1 to A7 cases, the amplitude of the spanwise pulsation is approximately constant, and the Stokes layer thickness is the only variable.

To analyze the effect of the prescribed excitation on the heat and momentum transport near the solid boundaries, two parameters, Thermal Enhancement Factor (TEF) and Shear Enhancement Factor (SEF), are introduced in order to measure the instantaneous changes in the skin friction coefficient and heat flux²⁸ as follows:

$$\text{SEF} = \frac{C_{f,\text{excited}}}{C_{f,\text{unexcited}}} \quad \text{and} \quad \text{TEF} = \frac{Nu_{\text{excited}}}{Nu_{\text{unexcited}}}, \quad (4)$$

where

$$C_f = \frac{\mu \frac{\partial U}{\partial y}|_{\text{wall}}}{0.5 \rho U_b^2} \quad \text{and} \quad Nu = \frac{\frac{\partial}{\partial y}(T - T_{\text{wall}})|_{\text{wall}}}{(T_b - T_{\text{wall}})/\delta}.$$

The history of these two quantities is plotted in Fig. 3 (left column).

In Fig. 3 (right column), δw is calculated at the channel center, where the viscous effect is minimal. The acceleration due to the spanwise pulsations during the first half of the period is wholly reversed during the second half. By contrast, the enhancement factors are a function of “shear stress” and “heat flux” compared to the unexcited profile, which are directed by the non-linear interaction between the “oscillating Stokes layer” and the “background turbulent structures” near the walls. Therefore, the enhancement factors exhibit a somewhat chaotic pattern, as in Fig. 3 (left).

Since the SEF and TEF remain equal over the entire duration of simulations, we conclude that, in this range of frequency and amplitude of excitation, there is a strong linear relationship between the heat and momentum transport in the boundary layer, suggesting that the *Reynolds Analogy* holds valid. Although not shown here, by increasing the amplitude, especially in low-frequency cases, such as A6 and A7, SEF and TEF begin to depart.³¹

At $t = 480$, all cases are at an identical phase, and considering the history of spanwise velocity perturbations, the transient regime ends before this instant. Therefore, this instance is selected to start the time-integration, which continues up to $t = 960$ where all cases again arrive at the same phase. If the time-integration begins later, the changes in $\overline{\text{TEF}}$ and $\overline{\text{SEF}}$ will be minimal, provided that a similar procedure is followed.

Time-averaged $\overline{\text{TEF}}$ is reported on each plot of Fig. 3 (left). The highest heat transfer reduction is achieved in A2 and A3 where $\mathcal{T} = 10$ and 20, resulting in 8% reduction of Nu as a result of spanwise acoustic excitation. According to Jung *et al.*¹ the excitation period can be non-dimensionalized with $\mathcal{T}^+ = \mathcal{T} u_\tau^2 / \nu$, and its optimal value for drag reduction in an incompressible channel is $\mathcal{T}^+ = 100$. This quantity in A2 and A3 cases is, respectively, $\mathcal{T}_{A2}^+ \approx 173$ and $\mathcal{T}_{A3}^+ \approx 346$ where ν is calculated at the wall. The difference is due to the non-uniform temperature and density profiles along the channel height seen in Fig. 2.

Taking $f^+ = 1/\mathcal{T}^+$, the time-averaged Nusselt number for this type of flow, at $Re_b = 3000$, can be approximated via

$$\overline{Nu} = \overline{Nu}_{\text{unexcited}} \left(1 - \frac{0.0011 \sqrt{f^+}}{f^+ - 49.35 \sqrt{f^+} + 790} \right). \quad (5)$$

The comparison between the DNS and approximated results is shown in Fig. 4.

The power required for the spanwise pulsation is calculated using

$$P_{\text{pulsation}} = \frac{L_x L_z}{t_f - t_i} \int_{t_i}^{t_f} \int_0^{L_y} f(t) \cdot w(y, t) \, dy dt, \quad (6)$$

where t_i and t_f represent the starting and final instance of time-integration. The amount of power saved through skin friction

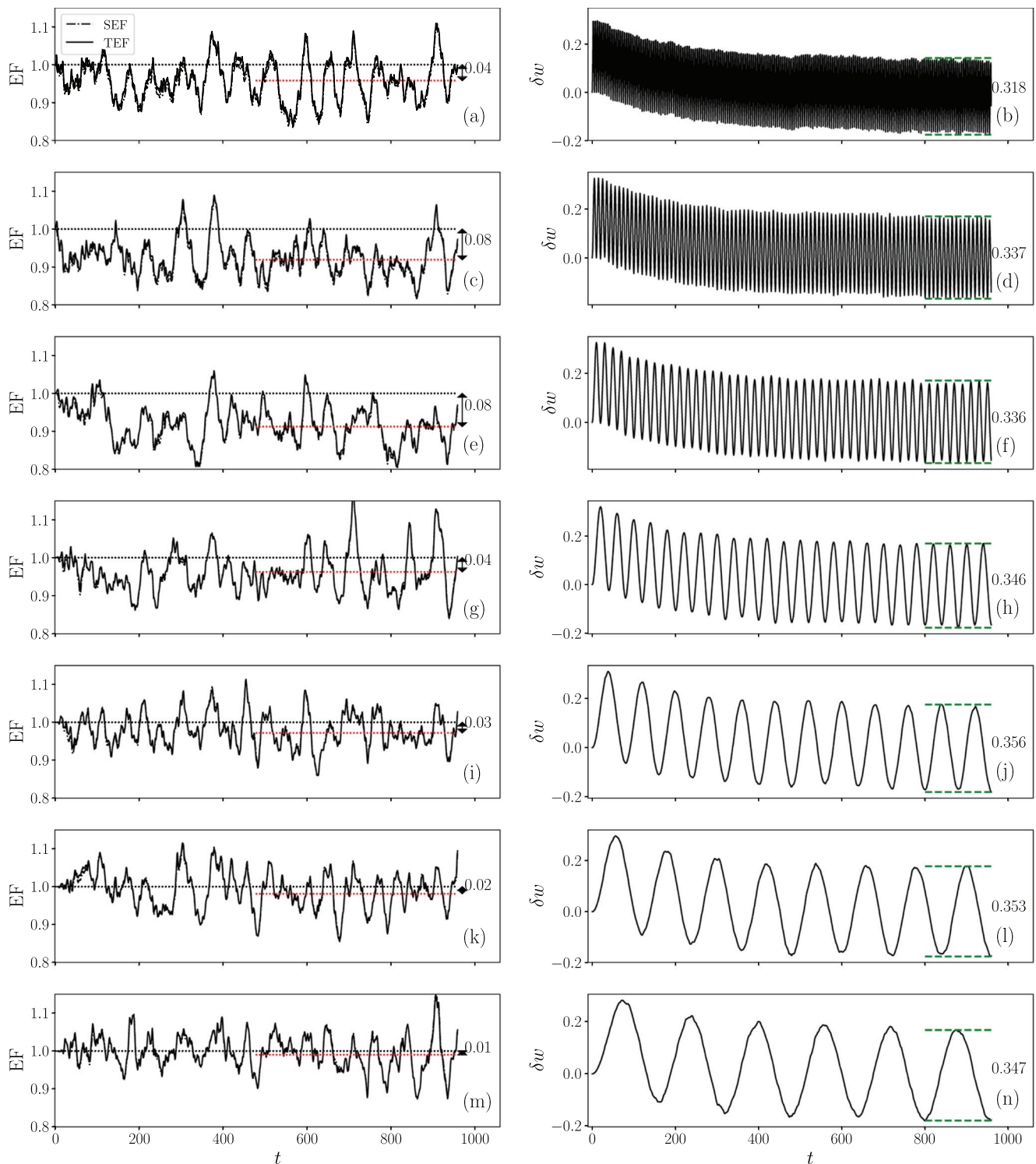


FIG. 3. History of the space-averaged TEF 4 (left) and spanwise velocity perturbations (δw) at the channel centers for cases A1: $\mathcal{F} = 5$ [(a) and (b)], A2: $\mathcal{F} = 10$ [(c) and (d)], A3: $\mathcal{F} = 20$ [(e) and (f)] as the reference, A4: $\mathcal{F} = 40$ [(g) and (h)], A5: $\mathcal{F} = 80$ [(i) and (j)], A6: $\mathcal{F} = 120$ [(k) and (l)], and A7: $\mathcal{F} = 160$ [(m) and (n)] at $Re_b = 3000$ and $M_{cl} = 1.49$. In all cases, the forcing amplitude is $A_f = 1/\mathcal{F}$. The wave-height (min-to-max value) corresponding to each case is also denoted on each plot. Time-averaged TEF taken during the limit-cycle oscillations is reported on all plots via a dashed-line (—), and the changes in this quantity due to excitation are printed on the graphs.

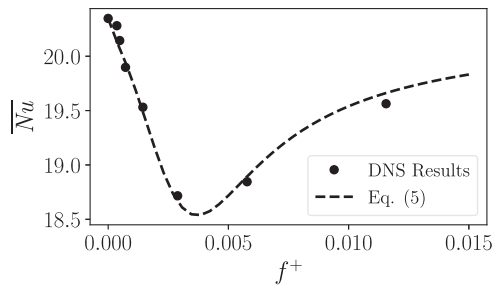


FIG. 4. Comparison between the approximated Nusselt number (Nu), via Eq. (5), against the DNS results.

reduction and heat transfer abatement from both walls, respectively, are determined as follows:

$$P_{\text{saved}} = \frac{2U_b L_x L_z}{t_f - t_i} \cdot \int_{t_i}^{t_f} \left(\mu \frac{\partial U}{\partial y} \Big|_{\text{wall, excited}} - \mu \frac{\partial U}{\partial y} \Big|_{\text{wall, unexcited}} \right) dt, \quad (7)$$

$$\dot{Q}_{\text{saved}} = \frac{2L_x L_z}{t_f - t_i} \cdot \int_{t_i}^{t_f} \left(k \frac{\partial T}{\partial y} \Big|_{\text{wall, excited}} - k \frac{\partial T}{\partial y} \Big|_{\text{wall, unexcited}} \right) dt. \quad (8)$$

These parameters are non-dimensionalized via the power required to maintain the constant mass flow-rate in the absence of any excitation:

$$P_{\text{flow}} = \frac{2U_b L_x L_z}{t_f - t_i} \int_{t_i}^{t_f} \mu \frac{\partial U}{\partial y} \Big|_{\text{wall, unexcited}} dt.$$

In the optimal configuration of A3, the power required to create the spanwise pulsation, $P_{\text{pulsation}}$, is 8.7% of the power supplied to sustain the mass flow-rate in the channel (P_{flow}), while the power saved as a result of skin friction reduction, P_{saved} , is 9.4% and heat transfer abatement, \dot{Q}_{saved} , is 14.6% of P_{flow} , therefore providing a net skin friction reduction and a substantial net heat transfer reduction. By increasing the excitation frequency, in case A2, which has the same TEF, $P_{\text{pulsation}}$ is

34.5% of the main power supplied, while the skin friction reduction, P_{saved} is 9.1% and \dot{Q}_{saved} is 13.6% of P_{flow} . On the other hand, by decreasing the excitation frequency, namely, in case A4, the required power for pulsation reduces to about 1.5%, and the saved power becomes P_{saved} 3.8% and \dot{Q}_{saved} 5.4% of P_{flow} . Hence, at a constant $A_f \mathcal{T}_f = 1$, the efficiency improves by decreasing the pulsation frequency; however, the total amount of drag and heat transfer reduction decreases.

B. Understanding the Stokes layer dynamics through the phase-locked and time-averaged statistics

In order to better characterize the Stokes layer created by the spanwise excitation, we decompose the instantaneous flow quantities into the time-averaged, harmonic, and random terms as follows:

$$q(\mathbf{x}, t) = \underbrace{\overline{q(\mathbf{x})}}_{\text{steady term}} + \underbrace{\widetilde{q(\mathbf{x}, t)}}_{\text{harmonic term}} + \underbrace{q'(\mathbf{x}, t)}_{\text{random fluctuation}}, \quad (9)$$

where the harmonic term is found from the phase-locked averaging at the excitation frequency ($\omega_f = 2\pi/\mathcal{T}$) over N excitation cycles:

$$\langle q(\mathbf{x}, t) \rangle = \frac{1}{N+1} \sum_{n=0}^N q(\mathbf{x}, t + n\mathcal{T}), \quad (10)$$

where

$$\widetilde{q(\mathbf{x}, t)} = \langle q(\mathbf{x}, t) \rangle - \overline{q(\mathbf{x})}.$$

This formulation is employed to extract the harmonic component of spanwise velocity in A1, A3, and A5 cases plotted in Fig. 5 at five instances of one excitation period. The viscous penetration length $l_{\text{visc}} = 2\pi\sqrt{2\nu_{\text{wall}}/\omega_f}$, calculated based on the viscosity at the wall, is also marked on the plots. This theoretical bound predicts the extent to which the viscous effects are relevant in the high and medium frequency cases. As displayed in Fig. 2, there is a large temperature gradient along the channel height, which results in an increase in the fluid viscosity from the walls to the channel center. At low frequency ($\mathcal{T} = 80$), where l_{visc} extends far into the channel core, the change of ν becomes more evident, and therefore, $l_{\text{visc}} = 2\pi\sqrt{2\nu_{\text{wall}}/\omega_f}$ only marks the lower bound of the viscous penetration length. The spanwise velocity perturbation near the Stokes layer thickness δ_s or $l_{\text{visc}}/2\pi$

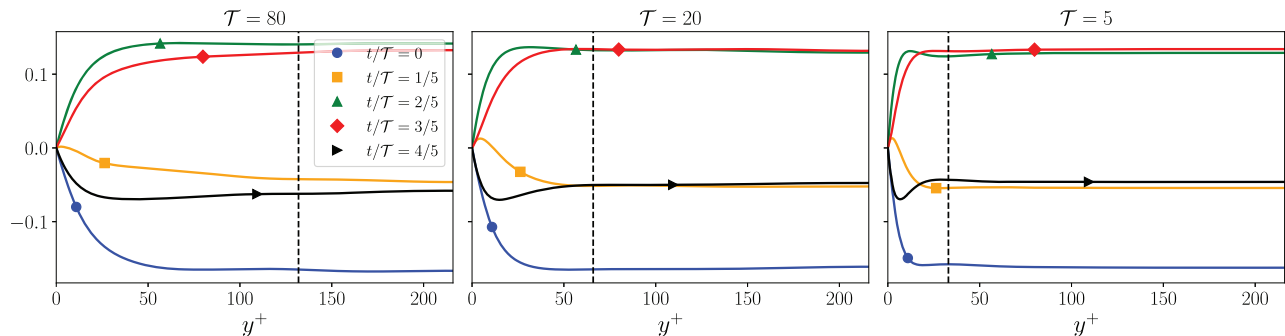


FIG. 5. Phase-locked averaged spanwise velocity \widetilde{W} at five different instances of one period (\mathcal{T}); excitation at (right) $\omega_f = 2\pi/80$, (middle) $\omega_f = 2\pi/40$, and (left) $\omega_f = 2\pi/20$. The vertical dashed-line (---) represents the viscous penetration length $l_{\text{visc}} = 2\pi\sqrt{2\nu_{\text{wall}}/\omega_f}$; (•) shows the starting phase of a period, i.e., $t/\mathcal{T} = 0/5$, (■) $t/\mathcal{T} = 1/5$, (▲) $t/\mathcal{T} = 2/5$, (◆) $t/\mathcal{T} = 3/5$, and (►) $t/\mathcal{T} = 4/5$.

overshoots the value at the channel core. This overshoot is most visible in the high-frequency case ($\mathcal{T} = 5$) and becomes weaker as the excitation period increases.

To better visualize the unsteady flow field, the space–time correlations of the spatially averaged harmonic terms, specifically the streamwise and spanwise velocity, as well as the harmonic temperature field, are plotted in Fig. 6. The vertical axis represents the wall-normal coordinates (y), and the horizontal axis indicates the phase of each time instance in the excitation cycle t/\mathcal{T} . Results corresponding to three excitation frequencies spanning $\mathcal{T} = 10$ to 80 are presented here. Red lines show the evolution of coherent perturbation created near the walls in the streamwise velocity and temperature, due to the spanwise pulsation. A strong coupling is observed between these quantities; \tilde{W} takes a simple sinusoidal form, with the wavenumber $k = 1$, in time. In accordance with Fig. 5's observation, the viscous effects become more confined to the wall by increasing the excitation frequency; a notably smaller dissipation of \tilde{W} is evident near the wall in high-frequency cases. The second row of Fig. 6 represents the time evolution of harmonic streamwise velocity \tilde{U} . A pattern with the wavenumber $k = 2$ can be clearly found near the wall in $\mathcal{T} = 10$ and $\mathcal{T} = 20$, while in the low-frequency case, the dominant wave number remains at $k = 1$. The magnitude of the streamwise velocity perturbations increases with a decrease in the excitation frequency. It is also evident that the non-linear interaction with the background turbulent flow is more pronounced in the low-frequency case. Since the period of excitation in this case, $\mathcal{T} = 80$, is significantly larger than the turbulent time-scale, the turbulent mixing further dissipates these perturbations as we near the channel core. The harmonic temperature component,

\tilde{T} , has a similar behavior as \tilde{U} in time, while the effect of pulsation is more confined to the wall.

All the cases studied in this section are conducted at one Mach and Reynolds number; consequently, non-dimensionalizing the statistical flow quantities based on wall quantities (of the unexcited case) reduces to linear scaling. To avoid over-complicating the presentation of results, we have expressed the results based on the original non-dimensionalization. However, the distance from the wall is shown by $y^+ = yu_\tau/\nu_{\text{wall}}$ to compare the Stokes layer thickness, given in the form of dimensional wall quantities in Table I, and the peak locations of different statistical quantities.

Due to the spanwise pulsations, “wall shear stress” deviates from the reference unexcited case and, subsequently, $u_{\tau, \text{excited}} = \sqrt{\tau_{\text{wall, excited}}/\rho_{\text{wall}}}$ takes different values in each case. Using $u_{\tau, \text{excited}}$ to calculate the viscous unit further complicates the representation of the results and, therefore, is avoided here.

1. First-order statistics

Subjected to the prescribed perturbations, the *acoustic streaming* appears in the flow that modifies the time-averaged velocity and temperature field. This concept is defined as follows:

$$q_{\text{st}} = \bar{q}_{\text{excited}} - \bar{q}_{\text{unexcited}}, \quad (11)$$

where \bar{q} represents a time-averaged quantity calculated during the limit-cycle oscillations (where $t > 480$).

Figure 7 displays the streaming velocity components in the spanwise and streamwise directions, as well as the streaming temperature profile. All the considered cases result in a similar distribution of U_{st}

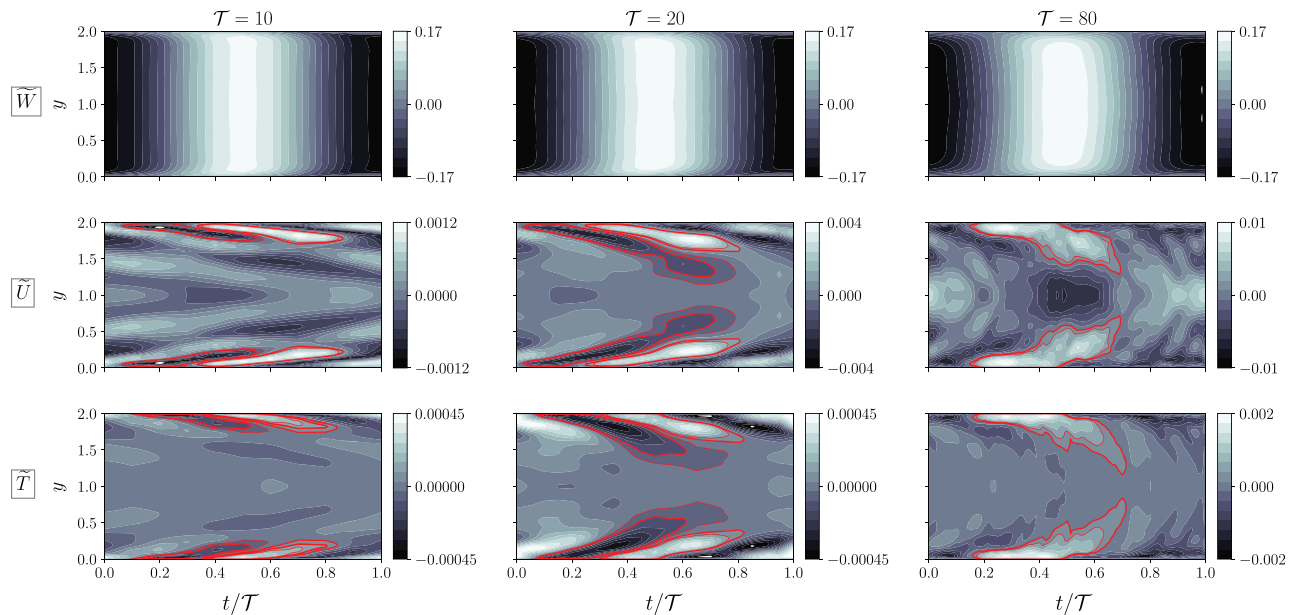


FIG. 6. Space–time correlation in the spanwise velocity, \tilde{W} (top row), streamwise velocity, \tilde{U} (middle row), and temperature, \tilde{T} (bottom row), for three different excitation frequencies, $\mathcal{T} = 10$ (first column), $\mathcal{T} = 20$ (second column), and $\mathcal{T} = 80$ (third column) at $Re_b = 3000$. Red lines show the evolution of coherent perturbation created in the streamwise velocity and temperature, due to the spanwise pulsation.

along the channel height; a non-zero streaming velocity appears near the wall, opposite to the flow direction. In other words, U_{st} indicates the streamwise velocity in the excited condition *relative* to the unexcited reference case. The negative value of this quantity does not imply a reverse flow, but instead specifies how the flow in streamwise direction slows down due to the pulsations. The magnitude of the streaming velocity, in all cases, decreases by approaching the channel center and may take small positive values. The negative peak's magnitude in the U_{st} profiles experiences its optimal value at the excitation period of $\mathcal{T} = 20$, corresponding to case A3. On the other hand, by reducing the excitation frequency, the negative peak's location moves slightly toward the channel center. The interplay of these two factors determines the slope of U_{st} at the wall, which in turn, indicates the drag reduction. This quantity takes similar values in cases A2 and A3, as it can be verified from the SEF in Fig. 3. Streaming temperature T_{st} also becomes negative near the wall, implying the cooling effect of the excitation, and the peak's magnitude reaches the optimal value at $\mathcal{T} = 20$. In this case, the peak's location is much closer to the wall, which was also observed in the harmonic temperature perturbations (comparing the second and third row in Fig. 6). This can be attributed to the steeper near-wall gradients observed in the unexcited mean flow temperature profile compared to the mean streamwise velocity. The streaming temperature profile near the channel center slightly increases by reducing the excitation frequency. Interestingly, at low frequencies, the excitation contributes to a more uniform heating of the flow across the channel height.

In contrast with U_{st} and T_{st} , the spanwise component of the streaming velocity, W_{st} , remains always positive, and the near-wall gradient is generally one order of magnitude smaller than the slope of U_{st} at the wall.

2. Second-order statistics

Streamwise, wall-normal, and spanwise normal Reynolds stress terms at different pulsation periods, namely, $\mathcal{T} = 5, 10, 20$ and 120 , are plotted in Fig. 8 (top). Profiles corresponding to the unexcited case, as the reference values, are also reported with dashed-lines. Given the level of \bar{W} , as in Fig. 5, we expect $\overline{w'w'}$ to undergo the most visible change due to the excitation; the peak values in all cases are more than twice larger than the peak

observed in the unexcited configuration. By increasing the excitation period, the peak's location moves slightly toward the channel center, as the Stokes layer (δ_s) thickens, as can be seen in Fig. 5. The main parameter in controlling the near-wall turbulence is the wall-normal stress, $\overline{v'v'}$, which, in this case, exhibits a significant reduction as a result of the spanwise excitation. This effect is translated into a reduction in $\overline{u'v'}$, specifically in its peak value, which also implies a decline in the shear stress. In agreement with the streaming velocity profiles (Fig. 7), as well as the skin friction reduction (manifested as the less-than-unity SEF in Fig. 3), the time statistics corresponding to the low-frequency case (for example, at $\mathcal{T} = 120$) experiences a minimal deviation from that of the unexcited configuration, and the optimal suppression of turbulent production is achieved at $\mathcal{T} = 10$ and $\mathcal{T} = 20$. This process can be attributed to the periodic re-alignment of the streamwise vortices and the near-wall streaks and disturbing the turbulence generation process discussed in Subsections III and IV. The impact of the spanwise excitation on the streamwise velocity perturbations, $\overline{u'u'}$, and temperature fluctuations, $\overline{T'T'}$, is similar; in both profiles, the peak's value decays due to the excitation. The minimum value is reached at $\mathcal{T} = 10$ and $\mathcal{T} = 20$, while the peak's location slightly moves toward the core. As such, there is a reduction in the turbulent heat flux, $\overline{T'v'}$. By tuning ω_f to the optimal range, an effective “skin friction” and “heat transfer” reduction can be achieved.

C. Turbulent kinetic energy and Reynolds shear stress transport analysis

We study the transport equation for the turbulent kinetic energy $K = \{u_j''u_j''\}/2$, where $\{\}$ represents the Favre-averaging (for a generic quantity $\{f\} = \overline{\rho f}/\overline{\rho}$ and $f = \{f\} + f''$), in order to further understand the mechanism of decay in heat and momentum transfer due to the spanwise pulsation. Following the work of Huang *et al.*³² and Pirozzoli *et al.*,³³ the transport equation is written as

$$\frac{\partial \overline{\rho k}}{\partial t} = -C + P + T + \Pi + D + D - \rho \epsilon, \quad (12)$$

where

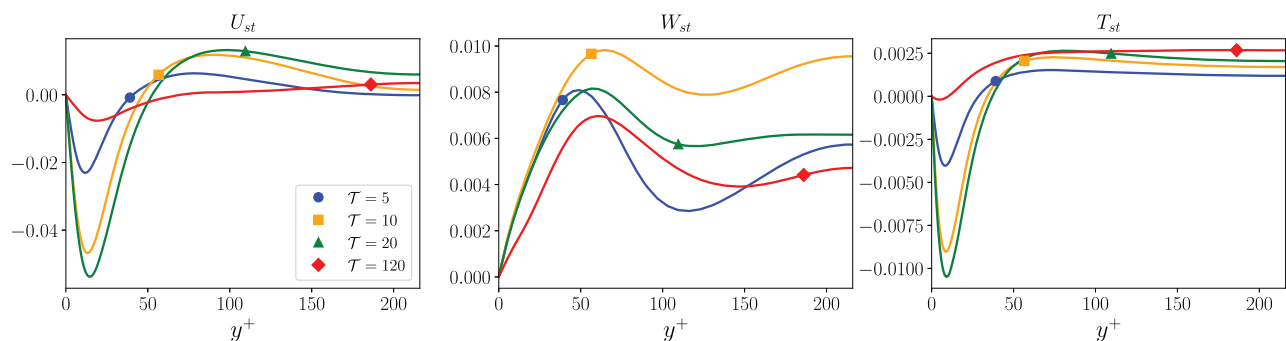


FIG. 7. Spatially averaged streaming velocity components in both streamwise (left) and spanwise (middle) directions along with the streaming temperature (right). Simulations are performed at $Re_b = 3000$ and $M_{cl} = 1.49$ subjected to the spanwise forcing of form (1) at $A_f \mathcal{T} = 1$: A1: $\omega_f = 2\pi/5$ and $A_f = 0.2$ (●), A2: $\omega_f = 2\pi/10$ and $A_f = 0.1$ (■), C1: $\omega_f = 2\pi/20$ and $A_f = 0.05$ (▲), and A5: $\omega_f = 2\pi/120$ and $A_f = 0.00834$ (◆).

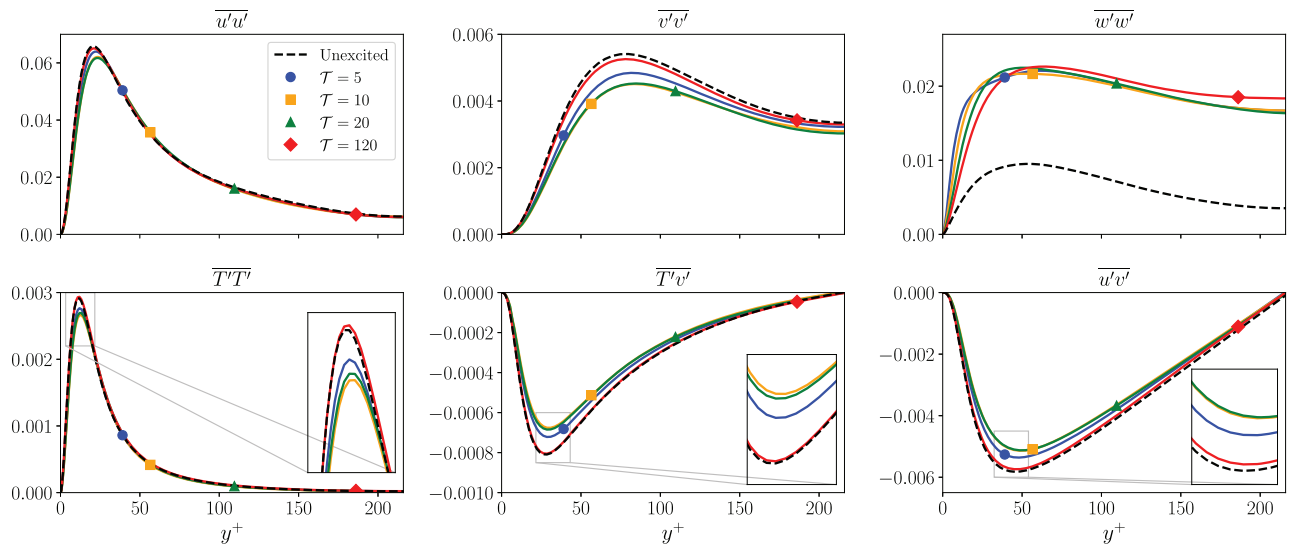


FIG. 8. Second-order turbulent statistics at $Re_b = 3000$ and $M_{cl} = 1.49$ subjected to the spanwise excitation at $A_f \mathcal{T} = 1$; unexcited case (---), A1: $\omega_f = 2\pi/5$ and $A_f = 0.2$ (●), A2: $\omega_f = 2\pi/10$ and $A_f = 0.1$ (■), A3: $\omega_f = 2\pi/20$ and $A_f = 0.05$ (▲), and A6: $\omega_f = 2\pi/120$ and $A_f = 0.00834$ (◆).

$$\begin{aligned}
 C &= \frac{\partial \bar{\rho} \{u_i\} K}{\partial x_j} && \text{convection,} \\
 P &= -\bar{\rho} \{u_i'' u_j''\} \frac{\partial \{u_i\}}{\partial x_j} && \text{production via mean velocity} \\
 &&& \text{gradients,} \\
 T &= -\frac{\partial}{\partial x_j} \left[\bar{\rho} \frac{\{u_i'' u_j'' u_k''\}}{2} + \overline{p' u_j'} \right] && \text{turbulent transport,} \\
 \Pi &= p' \frac{\partial u_i'}{\partial x_j} && \text{pressure dilatation,} \\
 M &= \bar{\rho} u_i'' \left(\frac{\partial \tau_{ij}}{\partial x_j} - \frac{\partial \bar{p}}{\partial x_i} \right) && \text{mass flux contribution due} \\
 &&& \text{to density fluctuations,} \\
 D &= \frac{\partial}{\partial x_j} \left(\tau_{ij}' u_j' \right) && \text{viscous diffusion,} \\
 \bar{\rho} \varepsilon &= \tau_{ij} \frac{\partial u_i'}{\partial x_j} && \text{molecular dissipation,}
 \end{aligned}$$

where τ_{ij} represents the instantaneous stress and ω_{ij}' is vorticity fluctuations $\omega_{ij}' = 1/2 (\partial u_i' / \partial x_j - \partial u_j' / \partial x_i)$. The dissipation term can be further decomposed into a solenoidal, $\bar{\rho} \varepsilon_s$, and dilatational $\bar{\rho} \varepsilon_d$, as well as an additional term, $\bar{\rho} \varepsilon_i$, to include the contribution of flow inhomogeneity. Figure 9 (left) illustrates the distribution of the right hand side terms in Eq. (12), normalized by $\bar{\tau}_{\text{wall}} \bar{U}_b / \delta$, as suggested by Huang *et al.*³² in the wall-normal direction for the unexcited case (A0). Convection (C), pressure dilatation (II), and the mass flux contribution due to density fluctuation (M) remain very small across the channel. The impact of spanwise excitation on these three terms is also negligible and, therefore, not discussed here. The other terms at four excitation frequencies are plotted on the right along with the unexcited case (represented by a dashed-line) as the reference.

As a result of the spanwise excitation, turbulent kinetic energy production via the gradients of the mean flow quantities decreases.

This can be seen in the form of a reduction in the peak of P . The largest decay is achieved at $\mathcal{T} = 10, 20$, and the corresponding location moves from $y^+ \approx 17.1$ to ≈ 18.7 . The energy produced in the buffer layer is partially dissipated here, and the rest is transferred to the viscous sub-layer and turned into heat there. This spatial re-distribution of K is carried out through the turbulent transport T , which consists of pressure-velocity fluctuation and velocity fluctuations, along with viscous diffusion D . In response to the spanwise excitation, both of these terms show a decay in their maximum values to account for the decreased turbulent kinetic energy production, most visibly in cases A1 and A2.

D. Near-wall turbulent structures

We use the instantaneous temperature field in order to identify the near-wall turbulent structures. Figure 10 (top section) displays the temperature fields near the bottom wall (at $y^+ \approx 5$) in the excited (case F1, $\omega_f = 2\pi/20$) and unexcited conditions (case F0) at four instances of a period at $Re_b = 3000$. The unexcited case (top row) shows a pack of low- and high-speed streamwise-oriented streaks, representing the classical pattern of a low-Reynolds turbulent flow field near the walls. Comparing the unexcited field against the spanwise excited temperature field (bottom row) suggests that the pulsation periodically disrupts the near-wall streaks by tilting them normal to the flow direction. In the high-Reynolds configuration, at $Re_b = 6000$ (bottom section), a similar response to the spanwise pulsation is observed; however, in some instances, the deflection appears to be more pronounced compared to the low-Reynolds number configuration. Overall, the density of the high-speed regions is visibly reduced by the excitation in cases F0 and F1, while this is as not obvious as when comparing the cases R0 and R3, suggesting that the former configuration has been more successful in heat transfer reduction.

The alignment of these near-wall streaks and the “quasi-streamwise” vortices (at $y^+ \approx 15$) is critical for the self-sustained turbulence generation.³⁴ The optimal spanwise pulsation should be able

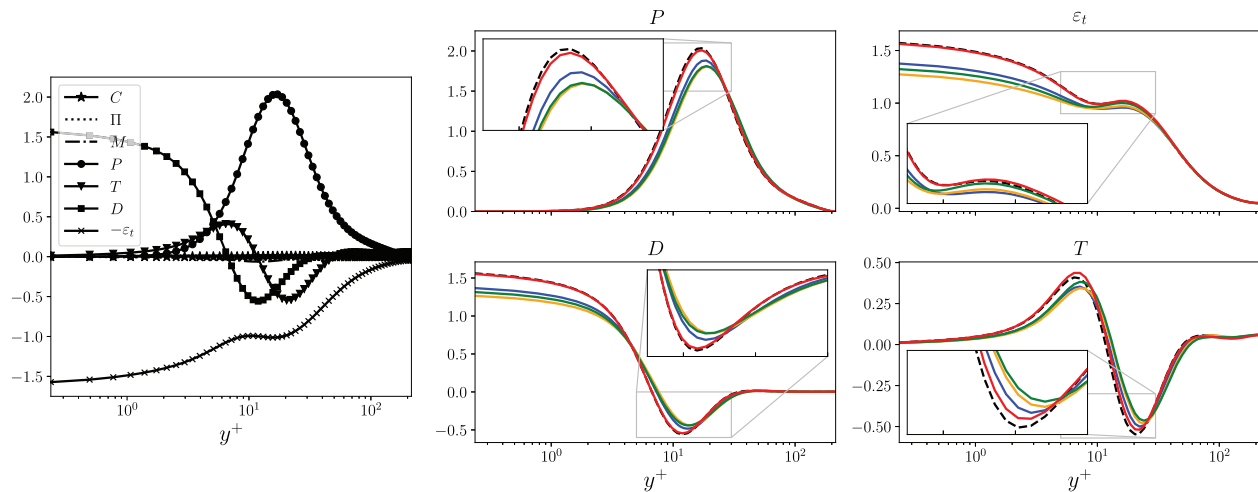


FIG. 9. Balance of turbulent kinetic energy $K = \{u_i' u_i'\}/2$ budget, normalized by $\bar{\epsilon}_{\text{wall}} \bar{U}_b / \delta$, at $Re_b = 3000$ and $M_{cl} = 1.49$ at four different excitation periods. On the left, all the RHS terms in Eq. (12) are plotted for the unexcited case to display the overall balance. On the right, the four significant terms, P , ϵ_t , D , and T , are shown. The insets magnify the buffer layer where $y^+ \in [5, 30]$. Line color legend is similar to that in Fig. 8.

to create a Stokes layer that effectively separates these two structures and create a slight mismatch between them in order to suppress the turbulence generation.³⁵ In order to quantitatively characterize the impact of the spanwise pulsation on the quasi-streamwise vortices, we

plot the pre-multiplied power spectra of the streamwise fluctuating velocity, $k_z E_{uu}$ in the spanwise direction. Figure 11 displays this parameter as a function of the dimensionless wall distance (y^+) and spanwise wavelength (λ_z^+). The top and bottom row, respectively,

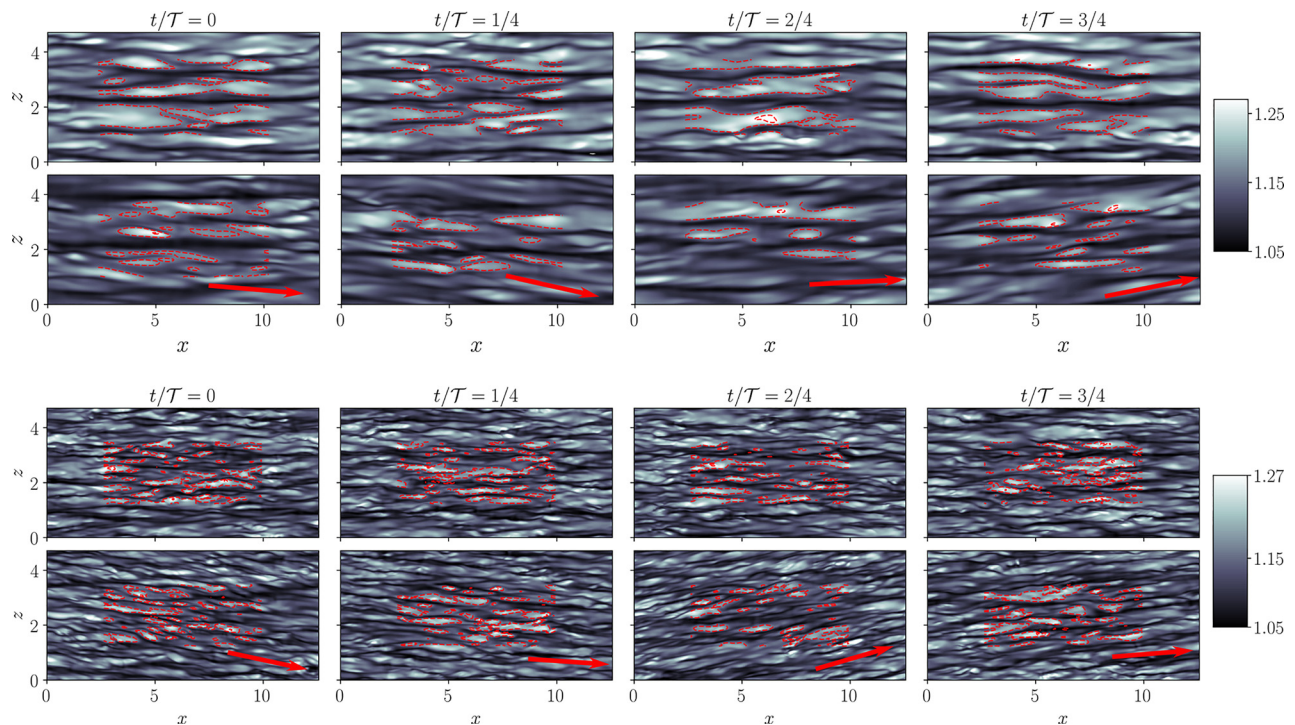


FIG. 10. Temperature fields near the bottom wall at $y^+ \approx 5$ at four different instances of one period, from left to right: at $t/\mathcal{T} = 0$, $t/\mathcal{T} = 1/4$, $t/\mathcal{T} = 2/4$, and $t/\mathcal{T} = 3/4$. The top section corresponds to the simulations performed at $Re_b = 3000$ and $M_{cl} = 1.49$. The top row represents the unexcited case (case F0), and the bottom row represent the excited case at $A_f = 0.05$ and $\mathcal{T} = 20$ (case F1). The bottom section is associated with the results of computations at $Re_b = 6000$ and $M_{cl} = 1.47$. The top row is the unexcited temperature field (R0), and the bottom is the outcome of the excitation at $A_f = 0.05$ and $\mathcal{T} = 20$ (R3). The edge of streaks, near the center of the plane, is marked with dashed red lines. Red arrows are guides to observe the tilting of the structures.

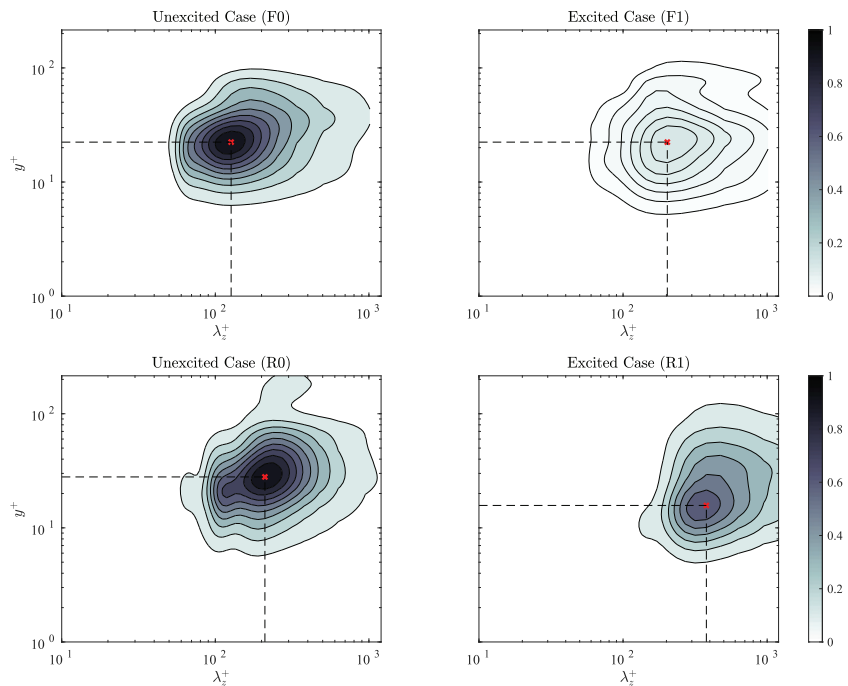


FIG. 11. Premultiplied energy spectrum of the streamwise velocity fluctuation, $k_z E_{uu}$, in terms of spanwise wavelength (λ_z^+) and wall distance (y^+), dimensionless by wall quantities, at $Re_b = 3000$ (top row) and $Re_b = 6000$ (bottom row). The left column is the unexcited (F0 and R0), and the right column represents the excited case (F1 and R1). The contours are normalized with the maximum value of the unexcited cases. The location of the maximum value is shown with \times .

indicate the low and high-Reynolds number cases. The left columns correspond to the unexcited configurations (cases F0 and R0), and the right columns are the outcomes of the optimal excitation (cases F1 and R1). The contour values are normalized with respect to the maxima in the unexcited cases. The spanwise pulsation significantly reduces the energy of the streamwise vortices.

This effect is clearly visible in the low-Reynolds number case, which is consistent with the decay seen in turbulent kinetic energy production P (see Fig. 9), as well as the subsequent decrease in turbulent heat flux ($\overline{T'v'}$) and the overall heat transfer abatement (about 8% seen in 4). The smaller P , moreover, results in a similar decrease in Reynolds shear stress ($\overline{u'v'}$) and the overall skin friction.

The vertical coordinate of the maximum energy indicates the mean position of the streamwise vortices away from the wall, and the horizontal coordinate shows the mean distance between two vortices in the spanwise direction.³⁶ As a result of the excitation, the

streamwise vortices are slightly moved toward the channel's center. This is seen in the peaks of P (in Fig. 9) and $\overline{T'T'}$ and $\overline{u'u'}$ (in Fig. 8). The mean spanwise distance of these vortices also increases substantially by about 60 wall units. Further analysis of one-dimensional pre-multiplied streamwise spectra of velocity fluctuations $k_x E_{uu}$ indicates that the spanwise pulsation does not change the mean streamwise spacing of near-wall large structures (λ_x^+) and their distance from the wall and only slightly reduces the amplitude of the energy peaks.

In the high-Reynolds number configuration, the maximum value of the streamwise vorticity still decays, due to the excitation, but to a smaller degree compared the low-Reynolds number case. This suggests a less effective reduction in the turbulent heat flux $\overline{T'v'}$ and Reynolds shear stress $\overline{u'v'}$, as shown in Fig. 12 (left and middle). Although the mean spanwise distance of the streamwise vortices increases substantially, the mean vertical location remains nearly unchanged as a result of the excitation.

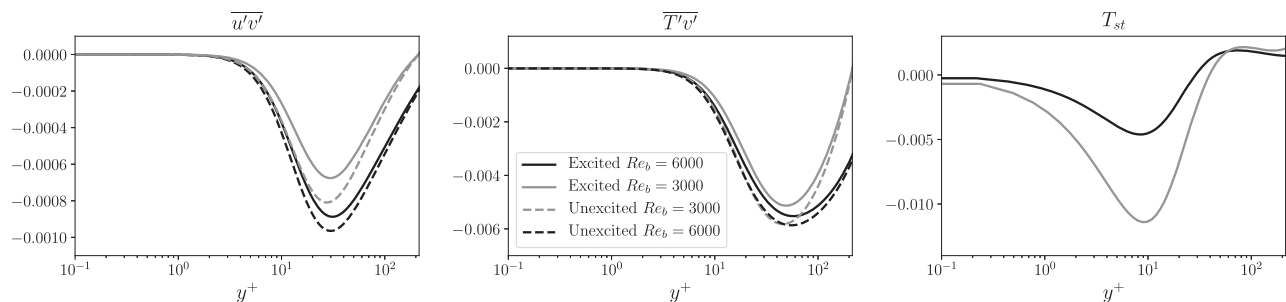


FIG. 12. The effect of the Reynolds number on the first- and second-order turbulent statistics. The excited configuration (solid line, cases F1 and R1) and unexcited configurations (---, F0 and R0) are compared at two Reynolds numbers $Re_b = 3000$ (gray) and $Re_b = 6000$ (black). Reynolds shear stress $\overline{u'v'}$ (left), turbulent heat flux $\overline{T'v'}$ (middle), and streaming temperature (right).

Overall, the configuration studied at the high Reynolds number delivers 4.5% heat transfer abatement, which is smaller than the low-Reynolds case of about 8%. The decay in effectiveness of spanwise pulsation by increasing the Reynolds number is consistent with the results of Ricco and Quadrio³⁷ for the spanwise wall oscillations. This effect is also reflected in the form of a smaller streaming temperature near the wall, plotted in Fig. 12 (right).

V. CONCLUSIONS

We study the response of a supersonic turbulent flow to the spanwise pulsation using a series of DNSs with the aim of heat transfer reduction. We observe that the oscillations periodically divert the near-wall turbulent structures in the spanwise direction and, therefore, disrupt the self-sustained turbulence generation in this region. This effect is characterized by a decay in the production term of turbulent kinetic energy, as well as turbulent heat flux and Reynolds shear stress. In this work, we only focus on the moderate levels of pulsation, where the amplitude of spanwise velocity oscillation at the channel center is $\tilde{W}_d \approx 12\%$ of bulk streamwise velocity or $\tilde{W}_d^+ \approx 2.0 - 2.2$. This limit is placed in order to avoid configurations with unreasonably high power requirements that dramatically degrade the efficiency of the entire system. At constant \tilde{W}_d , an optimal forcing frequency exists that delivers the largest heat transfer abatement, about 8%, at $Re_b = 3000$. By increasing the Reynolds number to $Re_b = 6000$ at an approximately constant \tilde{W}_d and Mach number M_{cb} , the effectiveness of the spanwise pulsation decays to about 4.5%.

In this paper, we studied the fundamental concept pertaining to heat transfer abatement via pulsating transverse forces. Future studies will focus on a parametric analysis over a wider range of Reynolds numbers, Mach numbers, and forcing amplitudes to derive a generic correlation for the Nusselt number for this flow configuration.

ACKNOWLEDGMENTS

The authors would like to thank Professor Sanjiva Lele for granting access to an early version of code CFDSU. This research was supported by the Binational Science Foundation (Grant No. 2016358) and the Office of Naval Research (Grant No. N00014-19-1-2433). Numerical simulations were performed, in part, on *Frontera* supercomputer at TACC through allocation ECS20002 and using the Extreme Science and Engineering Discovery Environment (XSEDE) Stampede2 at TACC and Bridges at PSC via allocations TG-CTS170041 and TG-CTS200027, as well as the AWS Cloud Credits for Research program.

NOMENCLATURE

(\prime)	turbulent fluctuations based on Favre-averaging
(\prime)	turbulent fluctuations based on Reynolds averaging
$(\prime)_d$	quantity at the channel center
$(\prime)_{\text{excited}}$	flow quantity in the presence of spanwise pulsation
$(\prime)_{\text{unexcited}}$	flow quantity in the unexcited case
$(\prime)_{\text{wall}}$	quantity at the wall
(\prime)	harmonic term = $\langle \prime \rangle - \overline{(\prime)}$
(\prime)	Reynolds averaging

$(\prime)_{\text{st}}$	streaming quantity = $(\prime)_{\text{excited}} - (\prime)_{\text{unexcited}}$
$\{\prime\}$	Favre-averaging = $\rho(\prime)/\bar{\rho}$
$\langle \prime \rangle$	phase-locked averaging
A_f	pulsation amplitude
E_{uu}	power spectra of streamwise velocity fluctuations
\tilde{f}_f	external force applied to the flow
k_z	wave number in the z -direction
l_{visc}	viscous penetration length = $2\pi\sqrt{2\nu_{\text{wall}}/\omega_f}$
Re_b	Reynolds number based on bulk velocity = $\rho_b U_b \delta / \mu_{\text{wall}}$
\mathcal{T}^+	dimensionless pulsation period based on wall quantities = $\mathcal{T} u_\tau^2 / \nu_{\text{wall}}$
\mathcal{T}	pulsation period = $2\pi/\omega_f$
U_b	bulk velocity = $\int_V \rho u dV / \int_V \rho dV$
τ_{wall}	wall shear stress
u_τ	friction velocity = $\sqrt{\tau_{\text{wall}}/\rho_{\text{wall}}}$
W^+	dimensionless spanwise velocity based on wall quantities = W/u_τ
y^+	dimensionless wall-normal coordinate based on wall quantities = $y u_\tau / \nu_{\text{wall}}$
δ	channel half-width
δ_s^+	dimensionless Stokes layer thickness on wall quantities = $y \delta_s u_\tau / \nu_{\text{wall}}$
δ_s	Stokes layer thickness = $\sqrt{2\nu_{\text{wall}}/\omega_f}$
λ_z^+	spanwise wavelength made dimensionless by wall quantities = $\lambda_z u_\tau / \nu_{\text{wall}}$
ρ_b	bulk density = $\frac{1}{V} \int_V \rho dV$
ω_f	pulsation frequency

DATA AVAILABILITY

The data that support the findings of this study are available from the corresponding author upon reasonable request.

REFERENCES

- W.-J. Jung, N. Mangiavacchi, and R. Akhavan, "Suppression of turbulence in wall-bounded flows by high-frequency spanwise oscillations," *Phys. Fluids A* **4**, 1605–1607 (1992).
- F. Laadhari, L. Skandaji, and R. Morel, "Turbulence reduction in a boundary layer by a local spanwise oscillating surface," *Phys. Fluids* **6**, 3218–3220 (1994).
- K.-S. Choi, J.-R. DeBisschop, and B. R. Clayton, "Turbulent boundary-layer control by means of spanwise-wall oscillation," *AIAA J.* **36**, 1157–1163 (1998).
- G. Karniadakis and K.-S. Choi, "Mechanisms on transverse motions in turbulent wall flows," *Annu. Rev. Fluid Mech.* **35**, 45–62 (2003).
- M. Quadrio, "Drag reduction in turbulent boundary layers by in-plane wall motion," *Philos. Trans. R. Soc., A* **369**, 1428–1442 (2011).
- J. Yao and F. Hussain, "Supersonic turbulent boundary layer drag control using spanwise wall oscillation," *J. Fluid Mech.* **880**, 388–429 (2019).
- T. W. Berger, J. Kim, C. Lee, and J. Lim, "Turbulent boundary layer control utilizing the Lorentz force," *Phys. Fluids* **12**, 631–649 (2000).
- K. S. Breuer, J. Park, and C. Henoch, "Actuation and control of a turbulent channel flow using Lorentz forces," *Phys. Fluids* **16**, 897–907 (2004).
- T. Jukes, K.-S. Choi, G. Johnson, and S. Scott, "Turbulent drag reduction by surface plasma through spanwise flow oscillation," in *3rd AIAA Flow Control Conference* (AIAA, 2006), p. 3693.
- P. Ricco and S. Hahn, "Turbulent drag reduction through rotating discs," *J. Fluid Mech.* **722**, 267–290 (2013).
- R. Akhavan, W. Jung, and N. Mangiavacchi, "Turbulence control in wall-bounded flows by spanwise oscillations," in *Advances in Turbulence IV* (Springer, 1993), pp. 299–303.

- ¹²M. Cannata, G. Cafiero, and G. Iuso, "Large-scale forcing of a turbulent channel flow through spanwise synthetic jets," *AIAA J.* **58**, 2042–2052 (2020).
- ¹³J. Sousa, G. Paniagua, and J. Saavedra, "Aerodynamic response of internal passages to pulsating inlet supersonic conditions," *Comput. Fluids* **149**, 31–40 (2017).
- ¹⁴N. Karamanis and R. F. Martinez-Botas, "Mixed-flow turbines for automotive turbochargers: Steady and unsteady performance," *Int. J. Engine Res.* **3**, 127–138 (2002).
- ¹⁵M. H. Padzillah, S. Rajoo, and R. F. Martinez-Botas, "Influence of speed and frequency towards the automotive turbocharger turbine performance under pulsating flow conditions," *Energy Convers. Manage.* **80**, 416–428 (2014).
- ¹⁶Z. Liu, J. Braun, and G. Paniagua, "Thermal power plant upgrade via a rotating detonation combustor and retrofitted turbine with optimized endwalls," *Int. J. Mech. Sci.* **188**, 105918 (2020).
- ¹⁷B. H. Saracoglu, G. Paniagua, S. Salvadori, F. Tomasoni, S. Duni, T. Yasa, and A. Miranda, "Trailing edge shock modulation by pulsating coolant ejection," *Appl. Therm. Eng.* **48**, 1–10 (2012).
- ¹⁸M. Quadrio and P. Ricco, "Critical assessment of turbulent drag reduction through spanwise wall oscillations," *J. Fluid Mech.* **521**, 251 (2004).
- ¹⁹M. V. Morkovin, "Effects of compressibility on turbulent flows," in *Mécanique de la Turbulence*, edited by A. Favre (CNRS, 1962), pp. 367–380.
- ²⁰C. Zhang, L. Duan, and M. M. Choudhari, "Direct numerical simulation database for supersonic and hypersonic turbulent boundary layers," *AIAA J.* **56**, 4297–4311 (2018).
- ²¹B. Wu, W. Bi, F. Hussain, and Z.-S. She, "On the invariant mean velocity profile for compressible turbulent boundary layers," *J. Turbul.* **18**, 186–202 (2017).
- ²²E. R. Van Driest, "Turbulent boundary layer in compressible fluids," *J. Aeronaut. Sci.* **18**, 145–160 (1951).
- ²³A. Trettel and J. Larsson, "Mean velocity scaling for compressible wall turbulence with heat transfer," *Phys. Fluids* **28**, 026102 (2016).
- ²⁴P. S. Volpiani, P. S. Iyer, S. Pirozzoli, and J. Larsson, "Data-driven compressibility transformation for turbulent wall layers," *Phys. Rev. Fluids* **5**, 052602 (2020).
- ²⁵G. N. Coleman, J. Kim, and R. D. Moser, "A numerical study of turbulent supersonic isothermal-wall channel flow," *J. Fluid Mech.* **305**, 159–183 (1995).
- ²⁶D. Modesti and S. Pirozzoli, "Reynolds and mach number effects in compressible turbulent channel flow," *Int. J. Heat Fluid Flow* **59**, 33–49 (2016).
- ²⁷T. Agarwal, I. Rahbari, J. Saavedra, G. Paniagua, and B. Cukurel, "Multifidelity analysis of acoustic streaming in forced convection heat transfer," *J. Heat Transfer* **142**, 021801 (2020).
- ²⁸I. Rahbari and G. Paniagua, "Acoustic streaming in turbulent compressible channel flow for heat transfer enhancement," *J. Fluid Mech.* **889**, A2 (2020).
- ²⁹S. Nagarajan, S. K. Lele, and J. H. Ferziger, "A robust high-order compact method for large eddy simulation," *J. Comput. Phys.* **191**, 392–419 (2003).
- ³⁰M. Allahyari, V. Esfahanian, and K. Yousefi, "The effects of grid accuracy on flow simulations: A numerical assessment," *Fluids* **5**, 110 (2020).
- ³¹I. Rahbari, "Acoustic streaming in compressible turbulent boundary layers," Ph.D. thesis, Purdue University, 2019.
- ³²P. G. Huang, G. N. Coleman, and P. Bradshaw, "Compressible turbulent channel flows: DNS results and modelling," *J. Fluid Mech.* **305**, 185–218 (1995).
- ³³S. Pirozzoli, F. Grasso, and T. B. Gatski, "Direct numerical simulation and analysis of a spatially evolving supersonic turbulent boundary layer at $M = 2.25$," *Phys. Fluids* **16**, 530–545 (2004).
- ³⁴J. Kim, "Physics and control of wall turbulence for drag reduction," *Philos. Trans. R. Soc., A* **369**, 1396–1411 (2011).
- ³⁵R. Akhavan, W. Jung, and N. Mangiavacchi, "Control of wall turbulence by high frequency spanwise oscillations," in *3rd Shear Flow Conference* (AIAA, 1993), p. 3282.
- ³⁶J. Jiménez, "The largest scales of turbulent wall flows," in *CTR Annual Research Briefs* (Stanford University, 1998).
- ³⁷P. Ricco and M. Quadrio, "Wall-oscillation conditions for drag reduction in turbulent channel flow," *Int. J. Heat Fluid Flow* **29**, 891–902 (2008).